Resolution Enhancement of Spatial Parametric Methods via Regularization

Gustavo Daniel Martín-del-Campo-Becerra, Sergio Alejandro Serafín-García, Andreas Reigber, *Fellow, IEEE*, Susana Ortega-Cisneros, and Matteo Nannini

***Abstract*—The spatial spectral estimation problem has applications in a variety of fields, including radar, telecommunications, and biomedical engineering. Among the different approaches for estimating the spatial spectral pattern, there are several parametric methods, as the well-known multiple signal classification (MUSIC). Parametric methods like MUSIC are reduced to the problem of selecting an integer-valued parameter [so-called model order (MO)], which describes the number of signals impinging on the sensors array. Commonly, the best MO corresponds to the actual number of targets, nonetheless, relatively large model orders also retrieve good-fitted responses when the data generating mechanism is more complex than the models used to fit it. Most commonly employed MO selection (MOS) tools are based on information theoretic criteria (e.g., Akaike information criterion, minimum description length and efficient detection criterion). Normally, the implementation of these tools involves the eigenvalues decomposition of the data covariance matrix. A major drawback of such parametric methods (together with certain MOS tool) is the drastic accuracy decrease in adverse scenarios, particularly, with low signal-to-noise ratio, since the separation of the signal and noise subspaces becomes more difficult to achieve. Consequently, with the aim of refining the responses attained by parametric techniques like MUSIC, this article suggests utilizing regularization as a postprocessing step. Furthermore, as an alternative, this article also explores the possibility of selecting a single relatively large MO (rather than using MOS tools) and enhancing via regularization, the solutions retrieved by the treated parametric methods. In order to demonstrate the capabilities of this novel strategy, synthetic aperture radar tomography is considered as application.**

***Index Terms*—Information criteria, maximum likelihood (ML), model order selection (MOS), regularization, synthetic aperture radar (SAR) tomography (TomoSAR).**

NOMENCLATURE

List of Acronyms

AIC	Akaike information criterion.
BMR	Bayes minimum risk.
DCRCB	Doubly constrained robust Capon beamforming.
DOA	Direction of arrival.
DR	Detection rate.
EDC	Efficient detection criterion.
EO	Equation of observation.
MAP	Maximum a posteriori probability.
MARIA	ML-inspired adaptive robust iterative approach.
MDL	Minimum description length.
ML	Maximum likelihood.
MO	Model order.
MOS	MO selection.
MSF	Matched spatial filtering.
MUSIC	Multiple signal classification.
PLOS	Perpendicular to the line-of-sight.
PSP	Power spectrum pattern.
RMSE	Root mean square error.
ROI	Region of interest.
SAR	Synthetic aperture radar.
SNR	Signal-to-noise ratio.
TomoSAR	SAR tomography.

Glossary of Notation

$\langle\cdot\rangle$	Averaging operator.
$\mathbf{D}(\mathbf{u})$	Diagonal matrix with vector $\mathbf{u}$ at the principal diagonal.
$\lvert\cdot\rvert$	Euclidean ℓ_2-norm.
$\mathrm{E}(\,)$	Expectation operator.
$^+$	Hermitian conjugate (adjoin).
$\mathbf{I}$	Identity matrix.
$\{\mathbf{U}\}_{\mathrm{diag}}$	Main diagonal of matrix $\mathbf{U}$.
$\perp$	Orthogonal.
$\ln\{\cdot\}$	Natural logarithm.
$^{\mathrm{T}}$	Transpose.
$\mathrm{tr}\{\mathbf{U}\}$	Trace of matrix $\mathbf{U}$.

Manuscript received July 30, 2021; revised September 27, 2021; accepted October 10, 2021. Date of publication October 14, 2021; date of current version November 17, 2021. (*Corresponding author: Gustavo Daniel Martín-del-Campo-Becerra.*)

Gustavo Daniel Martín-del-Campo-Becerra, Andreas Reigber, and Matteo Nannini are with the Microwaves and Radar Institute, German Aerospace Center, 82230 Oberpfaffenhofen, Germany (e-mail: gustavo.martindelcampobecerra@dlr.de; andreas.reigber@dlr.de; matteo.nannini@dlr.de).

Sergio Alejandro Serafín-García and Susana Ortega-Cisneros are with the Center for Research and Advanced Studies (Cinvestav), National Polytechnic Institute (IPN), 45019 Zapopan, Jalisco, Mexico (e-mail: sergio.serafin@cinvestav.mx; susana.ortega@cinvestav.mx).

Digital Object Identifier 10.1109/JSTARS.2021.3120281

I. INTRODUCTION

WITH the aim of locating the radiating (backscattering) sources by means of an array of sensors, the spatial spectral estimation problem consists on determining how the energy is distributed over space [1, Ch. 6]. This kind of problem has applications in a variety of fields, including radar [2], sonar [3], telecommunications [4], biomedical engineering [5], and seismology [6]. Among the different approaches for estimating the spatial spectral pattern, there are parametric and non-parametric methods, implemented within the DOA estimation framework.

Fig. 1. Proposed novel strategy.

Parametric methods as MUSIC assume that the spatial spectral pattern is composed of point-type-like radiating (backscattering) sources (targets), whose amount is smaller than the length of the acquired data [1, Ch. 5]. In this way, the spatial spectral estimation problem is reduced to the problem of selecting an integer-valued parameter (so-called MO), which describes the number of source signals impinging on the sensors array [1, Appendix C]. Additionally, these techniques assume a spatially white noise model [1, Ch. 6], required to guaranty the separation of the signal and noise subspaces.

A correct selection of the MO assures retrieving best possible (good-fitted) solutions. Generally, the best choice corresponds to the actual number of targets; conversely, MOs smaller than the actual number of targets produce underfitting, meaning that some of the actual targets are suppressed, as they are taken by noise. Models with relatively higher orders tend to retrieve good-fitted responses when the data generating mechanism is more complex than the models used to fit it [1, Appendix C]. Nonetheless, they may cause overfitting, meaning that the residual variation (i.e., noise) is considered as part of the recovered signal. Targets may appear where in reality there are none, causing false detections.

Most commonly employed MOS tools [7]–[9] are based on information theoretic criteria, e.g., AIC, MDL, and EDC. Normally, the implementation of these tools involves the eigenvalues decomposition of the data covariance matrix, besides of a priori information about the number of looks, which is not always known and needs to be estimated.

A major drawback of such parametric methods (together with certain MOS tool) is the drastic accuracy decrease in adverse scenarios, particularly, with low SNR, since the separation of the signal and noise sub-spaces becomes more difficult to achieve. Following this order of ideas, this article suggests utilizing regularization as a post-processing step, with the aim of refining the response attained by the treated parametric methods, especially, with low SNR. Furthermore, as an alternative, this article also explores the possibility of selecting manually a single relatively large MO (rather than using MOS tools) and enhancing via regularization, the solutions retrieved by the addressed parametric methods.

The proposed novel strategy is summarized in Fig. 1. First, a parametric focusing technique is defined (e.g., MUSIC); next, the corresponding MO is selected (e.g., via AIC, MDL, EDC or manually); finally, regularization is applied (e.g., MARIA) in order to refine the previously recovered solutions. MARIA [10], [11], is a statistical regularization method based on ML, which improves resolution significantly, performing suppression of artifacts and reduction of ambiguity levels.

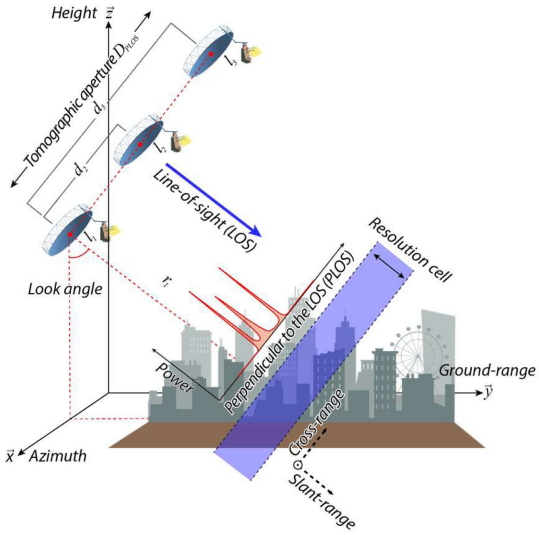

Fig. 2. TomoSAR acquisition geometry using parallel passes (not to scale).

One of the main advantages of regularization approaches like MARIA is their flexibility; in the sense that they can have as input, in principle, the retrievals of any parametric or non-parametric focusing technique. Previous related studies [10]–[13] utilize non-parametric methods as input (e.g., MSF, Capon beamforming, DCRCB, etc.). Yet, the usage of parametric techniques like MUSIC for such a purpose had not been studied yet. This article can therefore be understood as a complement of previously published studies.

In order to demonstrate the capabilities of the strategy depicted in Fig. 1, TomoSAR is considered as application. Its main goal is estimating the locations of the vertical structures that scatter the field back towards the (active) sensor. The TomoSAR inverse problem is typically defined via the linear EO [10]–[13]

$$\mathbf{y}_{[L\times 1]} = \mathbf{A}_{[L\times M]}\mathbf{s}_{[M\times 1]} + \mathbf{n}_{[L\times 1]}. \tag{1}$$

As depicted in Fig. 2, the TomoSAR acquisition constellation consists of L tracks (passes), each one with a different line-of-sight. One co-registered SAR image is collected from each pass; afterwards, the imagery is coherently combined using SAR interferometric techniques. Assuming co-registration independent on height, these L passes are treated as a linear sensors array. Accordingly, for a given azimuth-range position, vector $\mathbf{y}$ represents the set of L processed signals; vector $\mathbf{s}$ gathers M samples of the complex random reflectivity, taken at the PLOS elevation positions $\{z_m\}_{m=1}^{M}$; and vector $\mathbf{n}$ accounts for the additive noise. The $L \times M$ steering matrix $\mathbf{A}$ is the signal formation operator that maps $S \to Y$, the source Hilbert signal space S onto the observation Hilbert signal space Y.

The TomoSAR problem consists on estimating the PSP (in the PLOS height direction) for each azimuth-range location within the illuminated region. The PSP is depicted in a discrete

form through vector $\mathbf{b} = \{b_m\}_{m=1}^{M} = \{\langle |s_m|^2 \rangle\}_{m=1}^{M}$, i.e., the second-order statistics of the complex reflectivity vector $\mathbf{s}$.

The rest of this article is organized as follows: the TomoSAR signal model is presented in Section II. Section III describes MUSIC. Section IV reviews the different treated MOS tools. Section V addresses MARIA. Section VI analyses the proposed novel strategy through numerical examples. Section VII presents experimental results using real data, acquired from an urban test site. Finally, Section VIII concludes this article.

II. TomoSAR Signal Model

Refer to EO in (1), matrix $\mathbf{A}$ is composed of M steering vectors, each one of dimension L. The steering vectors $\{\mathbf{a}_m\}_{m=1}^{M}$ contain the interferometric phase information associated to the sources located along the PLOS elevation positions $\{z_m\}_{m=1}^{M}$, above the reference focusing plane. For a specified PLOS elevation position z, the related steering vector is given by [10], [14], [15],

$$\mathbf{a}(z) = \left[1 \quad \exp\{\mathrm{j}k_{z2}z\} \quad \cdots \quad \exp\{\mathrm{j}k_{zL}z\}\right]^{\mathrm{T}}, \tag{2}$$

in which

$$\left\{k_{zl} = \left(\frac{4\pi}{\lambda}\right)\left(\frac{d_l}{r_1 \sin\theta}\right)\right\}_{l=2}^{L} \tag{3}$$

is the two-way vertical wavenumber between the master track and the lth acquisition position. The slant-range distance to a particular target is defined by r_1, whereas $\{d_l\}_{l=2}^{L}$ is the cross-range oriented baseline between the master position and the lth acquisition position (see Fig. 2); with λ standing for the carrier wavelength and θ representing the incidence angle.

The complex random Gaussian zero-mean vectors $\mathbf{n}$, $\mathbf{s}$ and $\mathbf{y}$ are characterized by their corresponding correlation matrices

$$\mathbf{R_n} = \mathrm{E}\left(\mathbf{n}\mathbf{n}^{+}\right) = N_0\,\mathbf{I}, \tag{4}$$

$$\mathbf{R_s} = \mathrm{E}\left(\mathbf{s}\mathbf{s}^{+}\right) = \mathbf{D}(\mathbf{b}), \tag{5}$$

and

$$\mathbf{R_y} = \mathrm{E}\left(\mathbf{y}\mathbf{y}^{+}\right) = \mathbf{A}\mathbf{R_s}\mathbf{A}^{+} + \mathbf{R_n}, \tag{6}$$

where N_0 is the power spectral density of the white noise power [15] and vector $\mathbf{b}$ defines the backscattering power for a specified azimuth-range position, the so-called PSP. Entries of vector $\mathbf{s}$ are assumed uncorrelated, which simplifies the mathematical developments that led to MUSIC [1, eq. (4.2.7)] and MARIA [10], [11].

The (measured) data covariance matrix is defined by

$$\mathbf{Y} = \frac{1}{J}\sum_{j=1}^{J} \mathbf{y}_{(j)}\mathbf{y}_{(j)}^{+}, \tag{7}$$

where J indicates the amount of looks (independent realizations) of the signal acquisitions. The usage of the data covariance matrix for focusing is aimed to handle multiple nondeterministic sources, besides of increasing accuracy in presence of signal-dependent (multiplicative) noise [16, Ch. 18].

For each azimuth-range position within the illuminated area, given the data recordings $\mathbf{y} = \{y_l\}_{l=1}^{L}$, the steering matrix $\mathbf{A}$ and some prior knowledge on the problem (e.g., about the statistics of the signal and noise), the nonlinear TomoSAR inverse problem consists in estimating the actual PSP vector $\mathbf{b} = \{\langle |s_m|^2 \rangle\}_{m=1}^{M}$. The TomoSAR problem is ill-conditioned, since it does not accomplish the *uniqueness* Hadamard condition [16, Ch. 15]. The number of samples M is (much) larger than the number of data recordings L, therefore, there are an infinite number of possible solutions. Hence, by making some appropriate assumptions and/or by imposing some form of constraints, the different focusing techniques must guarantee retrieving well-conditioned solutions to the nonlinear TomoSAR inverse problem.

III. Multiple Signal Classification

Estimating the continuous PSP from a finite number of observations is an ill-posed problem in the Hadamard sense, unless proper assumptions are made. In order to overcome this problem, parametric methods as MUSIC parameterize the PSP by means of a finite dimensional model [1, Ch. 5].

Assume n point-type-like targets placed at the PLOS elevation positions $\{\dot{z}_n\}_{n=1}^{N}$. The number of targets n is smaller than the number of data acquisitions L. The noise $\mathbf{n}$ in EO is assumed spatially white with components having identical variance N_0. The signal correlation matrix $\mathbf{R_s}$ is assumed nonsingular. Finally, the signals and noise are assumed uncorrelated with one another [1, Ch. 6].

Let $[\varrho_1 \geq \varrho_2 \geq \ldots \geq \varrho_L]$ denote the eigenvalues of the modeled data covariance matrix $\mathbf{R_y}$, arranged in decreasing order. All L corresponding eigenvectors are orthogonal to each other, since $\mathbf{R_y}$ is Hermitian. The subset of eigenvectors $\mathbf{Q} = [\mathbf{q}_1 \quad \mathbf{q}_2 \quad \ldots \quad \mathbf{q}_n]$, related to the first n largest eigenvalues, spans the signal subspace; whereas $\mathbf{G} = [\mathbf{g}_1\ \mathbf{g}_2\ \ldots\ \mathbf{g}_{L-n}]$, related to the remaining $L-n$ eigenvalues, spans the noise subspace.

The signal subspace is orthogonal to the noise subspace, $\mathbf{Q} \perp \mathbf{G}$, meaning that any steering vector $\mathbf{a}$ residing in $\mathbf{Q}$ is orthogonal to $\mathbf{G}$. Therefore, if $\mathbf{a} \in \mathbf{Q}$ then $\mathbf{G}^{+}\mathbf{a}^2 = \mathbf{a}^{+}\mathbf{G}\mathbf{G}^{+}\mathbf{a} = 0$. The noise subspace $\mathbf{G}$ contains then complete information about the DOAs. Consequently, the locations of the addressed point-type-like targets are determined as the n highest peaks of the expression [1, eq. (4.5.15)]

$$\left\{\hat{b}_m = \frac{1}{\mathbf{a}_m^{+}\mathbf{G}\mathbf{G}^{+}\mathbf{a}_m}\right\}_{m=1}^{M} \tag{8}$$

with $\mathbf{G}\mathbf{G}^{+}$ as the so-called noise subspace covariance matrix.

In practice, $\mathbf{R_y}$ is estimated through the data covariance matrix $\mathbf{Y}$ in (7), whereas n refers to the MO to be selected, e.g., via AIC, MDL, EDC or manually.

IV. Model Order Selection

The ML method of parameter estimation is the basis of MOS rules as AIC, MDL and EDC. Aimed at estimating the MO, it refers to the optimization problem defined by [1, eq. (C.2.1)]

$$\hat{\varphi} = \underset{\varphi}{\operatorname{argmax}}\left\{\ln\left\{p\left(\mathbf{y}\,|\varphi(n)\right)\right\}\right\}. \tag{9}$$

For the case of MUSIC, vector $\varphi(n) = \{\varrho_k\}_{k=1}^{n}$ gathers the eigenvalues of $\mathbf{R_y}$, arranged in decreasing order, with $n \in \{1, 2, .., L\}$.

Being vector $\mathbf{y}$ in EO a L-dimensional complex random Gaussian zero-mean vector, it is explicitly characterized through its *probability density function* via [10], [17],

$$p(\mathbf{y}) = \pi^{-L} \det{}^{-1}\{\mathbf{R_y}\} \cdot \exp\left\{-\left(\mathbf{y}^{+}\mathbf{R_y}^{-1}\mathbf{y}\right)\right\}. \quad (10)$$

The MAP approach [17, Ch. 8] for solving the TomoSAR problem is given by

$$\hat{\mathbf{b}} = \underset{\mathbf{b}}{\operatorname{argmax}} \{\ln\{p(\mathbf{b}|\mathbf{y})\}\} \quad (11)$$

with

$$\ln\{p(\mathbf{b}|\mathbf{y})\} = \ln\{p(\mathbf{y}|\mathbf{b})\} + \ln\{p(\mathbf{b})\} - \ln\{p(\mathbf{y})\}, \quad (12)$$

according to the Bayes formula and since $\ln\{\cdot\}$ is a monotonically increasing function. Setting $p(\mathbf{b}) \approx \text{const}$, since it is unknown, and ignoring those terms that do not comprise $\mathbf{b}$ in (12), the log-likelihood function is defined as

$$\ln\{p(\mathbf{y}|\mathbf{b})\} = -\ln\{\det\{\mathbf{R_y}\}\} - \mathbf{y}^{+}\mathbf{R_y}^{-1}\mathbf{y}. \quad (13)$$

In order to express (13) as required by (9), the modeled data covariance matrix $\mathbf{R_y}$ in (6) must be represented as function of $\varphi(n)$ instead of $\mathbf{b}$, as described by [8, (eq. 9)]

$$\mathbf{R_y} = \sum_{k=1}^{n} (\varrho_k - N_0)\, \mathbf{q}_k \mathbf{q}_k^{+} + \mathbf{R_n}, \quad (14)$$

where n is the MO. Using the following property

$$\mathbf{y}^{+}\mathbf{R_y}^{-1}\mathbf{y} = \operatorname{tr}\left\{\mathbf{R_y}^{-1}\mathbf{y}\mathbf{y}^{+}\right\}, \quad (15)$$

the log-likelihood function in (13) is then expressed as

$$\ln\{p(\mathbf{y}|\varphi(n))\} = -J \cdot \ln\{\det\{\mathbf{R_y}\}\} - \operatorname{tr}\left\{\mathbf{R_y}^{-1}\mathbf{Y}\right\} \quad (16)$$

with $\mathbf{Y}$ as defined in (7). Recall that J is the number of independent observations.

The ML estimate $\hat{\varphi}$ in (9) is the value of $\varphi(n)$ that maximizes (16). Following [8, (eq. 14)], after some manipulations, the log-likelihood function is approximated through

$$\ln\{p(\mathbf{y}|\varphi(n))\} = \ln\left\{\frac{\prod_{k=n+1}^{L} \varrho_k{}^{\frac{1}{L-n}}}{\frac{1}{L-n}\sum_{k=n+1}^{L}\varrho_k}\right\}^{(L-n)J}, \quad (17)$$

this time with $\varphi(n) = \{\varrho_k\}_{k=n+1}^{L}$ and $n \in \{1, 2, .., L-1\}$.

A. Akaike Information Criterion

The AIC MOS rule maximizes the Kullback-Leibler information criterion [7]

$$\int p(\mathbf{y}) \ln\left\{\frac{p(\mathbf{y})}{p(\mathbf{y}|\varphi(n))}\right\} d\mathbf{y} \quad (18)$$

given the several hypotheses $\varphi(n)$. For the addressed problem, AIC consists in minimizing the next function [8], [9],

$$\begin{aligned}\operatorname{AIC}(\varphi(n)) = &-\ln\{p(\mathbf{y}|\varphi(n))\} + n(2L-n); \\ &n \in \{1, 2, .., L-1\}. \end{aligned} \quad (19)$$

B. Minimum Description Length

Proposed by Van Trees [18], MDL selects the MO that yields the MAP. Based on Bayesian arguments, a prior probability is assigned to each competing MO. As with AIC, MDL consists in minimizing the function

$$\begin{aligned}\operatorname{MDL}(\varphi(n)) = &-\ln\{p(\mathbf{y}|\varphi(n))\} \\ &+ \frac{1}{2} n(2L-n) \cdot \ln\{J\}; \\ &n \in \{1, 2, .., L-1\}. \end{aligned} \quad (20)$$

C. Efficient Detection Criterion

Developed at the University of Pittsburg [9], EDC minimizes the expression

$$\begin{aligned}\operatorname{EDC}(\varphi(n)) = &-\ln\{p(\mathbf{y}|\varphi(n))\} \\ &+ n(2L-n) \cdot C(J); \\ &n \in \{1, 2, .., L-1\}; \end{aligned} \quad (21)$$

where $C(J)$ is any function of J such that

$$\lim_{J\to\infty} \frac{C(J)}{J} = 0; \ \lim_{J\to\infty} \frac{C(J)}{\ln\{\ln\{J\}\}} = \infty. \quad (22)$$

In this article, we consider $C(J) = \sqrt{J \cdot \ln\{J\}}$.

For all addressed MOS tools (i.e., AIC, MDL and EDC), the second term at right hand, so-called penalty term, is intended to prevent selecting the largest MOs, with the aim of avoiding overfitting. As you can observe, the penalty term distinguishes one MOS rule from another.

V. ML-Inspired Adaptive Robust Iterative Approach

Regularization approaches are widely used to solve linear problems as the one given in EO, see [20], [21], and the references therein. The retrieval of well-conditioned solutions (in the Hadamard sense [16, Ch. 15]) is accomplished by providing smoothing into the solution and by incorporating known properties of the solution into the solver. In this way, the ill-conditioned problem is replaced with a well-posed optimization problem.

In previous related studies [10]–[13], [22], [23], different statistical regularization techniques are extended to cope with nonlinear ill-posed inverse problems, which is the case of TomoSAR. Among them, we find MARIA, an iterative statistical regularization method that performs resolution enhancement, suppression of artifacts and reduction of ambiguity levels [11].

MARIA provides an approximate solution to the ML optimization problem in (13) via

$$\hat{\mathbf{b}}_{\text{MARIA}}^{[i+1]} = \mathbf{T}^{[i]}\left[\hat{\mathbf{b}}_{\text{BMR}}^{[i]} - \mathbf{w}^{[i]}\right]; \ i = 0, 1, \ldots, I; \quad (23)$$

where vector $\hat{\mathbf{b}}_{\text{BMR}}^{[i]} = \{\mathbf{F}_{\text{BMR}}^{[i]} \mathbf{Y} \mathbf{F}_{\text{BMR}}^{[i]+}\}_{\text{diag}}$ is recognized as the BMR estimate of the PSP. The subtraction of the bias vector $\mathbf{w}^{[i]} = \{\mathbf{F}_{\text{BMR}}^{[i]} \mathbf{R_n} \mathbf{F}_{\text{BMR}}^{[i]+}\}_{\text{diag}}$ from $\hat{\mathbf{b}}_{\text{BMR}}^{[i]}$ corrects the shift due to the noise in the observed data, whereas the diagonal matrix $\mathbf{T}^{[i]} = \mathbf{D}(\{\mathbf{A}^{+}\mathbf{F}_{\text{BMR}}^{[i]+}\mathbf{F}_{\text{BMR}}^{[i]}\mathbf{A}\}_{\text{diag}})$ is an adaptive window operator that provides smoothing to the already rectified

BMR estimate. The solution operator is defined as

$$\mathbf{F}_{\mathrm{BMR}}^{[i]} = \mathbf{D}\left(\hat{\mathbf{b}}^{[i]}\right)\mathbf{A}^{+}\mathbf{R}_{\mathbf{y}}^{-1}. \tag{24}$$

In order to construct the matrices $\mathbf{D}(\hat{\mathbf{b}}^{[0]})$ and $\mathbf{R}_{\mathbf{y}} = \mathbf{A}\mathbf{D}(\hat{\mathbf{b}}^{[0]})\mathbf{A}^{+} + N_0\mathbf{I}$, a first estimate of the PSP $\hat{\mathbf{b}}^{[0]}$ is required. The dependence on a first estimate $\hat{\mathbf{b}}^{[0]}$ implies that no unique regularization method to recover $\hat{\mathbf{b}}_{\mathrm{MARIA}}$ exists. Different solutions are retrieved for different initial estimates $\hat{\mathbf{b}}^{[0]}$, especially when the discrepancies between them are highly significant. Yet, the adaptive iterative implementation of MARIA alleviates the issue in certain extent.

In this article, the first estimate $\hat{\mathbf{b}}^{[0]}$ is computed using MUSIC in (8), selecting the MO via AIC, MDL, EDC or manually. Afterwards, MARIA refines the estimates $\hat{\mathbf{b}}^{[i]}$ of each iteration, until achieving convergence $\hat{\mathbf{b}}_{\mathrm{MARIA}}^{[i=I]}$. In practice, the iterative procedure is finished either by reaching a maximum number of iterations or a user tolerance control level.

Factor N_0 in $\mathbf{R}_{\mathbf{y}}$ in (6) acts as a diagonal-loading regularization parameter, which assures matrix $\mathbf{R}_{\mathbf{y}}$ to be invertible. The proper choice of this regularization parameter guarantees retrieving good-fitted (well-regularized) reconstructions. In order to select the regularization parameter $\xi = N_0$, the L-Curve method is employed. Detailed in [12], the *L*-curve method seeks a balance between the norm of a penalty term and the norm of the residual. Basically, it consists in forming a smooth curve by plotting the points

$$L_C(\xi_n) = \left[\ln\left\{\left\|\mathbf{A}\hat{\mathbf{s}}(\xi_n) - \mathbf{y}\right\|\right\}, \ln\left\{\left\|\hat{\mathbf{s}}(\xi_n)\right\|\right\}\right] \tag{25}$$

for a collection of candidates $\{\xi_n\}_{n=1}^{N}$ with $\{\hat{\mathbf{s}}(\xi_n) = \mathbf{F}_{\mathrm{BMR}}(\xi_n)\mathbf{y}\}_{n=1}^{N}$. The resultant curve has the shape of a letter *L*, with a smooth corner; the proper value for $\xi = N_0$ is found as near as possible to this corner.

VI. Simulation Results

This section analyses the capabilities of the proposed novel strategy depicted in Fig. 1. As explained previously, parametric techniques as MUSIC assume a PSP composed of a finite number of point-type-like backscattering sources. Therefore, due to the characteristics of MUSIC, we refer to an urban-like scenario with three point-type-like targets.

We consider an *L*-band SAR sensor (0.23 m wavelength) at a nominal altitude of 3000 m. The acquisition geometry consists of 7 evenly distributed passes (flight tracks) spanning a PLOS synthetic aperture (see Fig. 2) of 60 m. For a slant-range distance from the targets to the master track of about 4000 m, the attained Fourier resolution [12] is approximately 7.5 m.

Data covariance matrices $\mathbf{Y}$ in (7) serve as input to the MUSIC and MARIA focusing techniques. Constructed with $J = 300$ independent looks, these matrices gather the echoes of the scatterers displaced along the PLOS height direction. The simulated scene comprises three point-type-like targets, each composed of 100 scatterers with equal reflectivity, following narrow Gaussian distributions. The phase-centers (mean heights) are placed at $\dot{z}_1 = -2$ m, $\dot{z}_2 = 0$ m and $\dot{z}_3 = 3$ m, respectively, with spreads (standard deviation) of 0.01 m. The usage of Gaussian distributions is due to its practicality for incorporating statistical uncertainty to the measurements via random fluctuations of each independent look. In this way, we do not only rely on additive noise to introduce decorrelation. Furthermore, the location of the phase-centers matches the mean values.

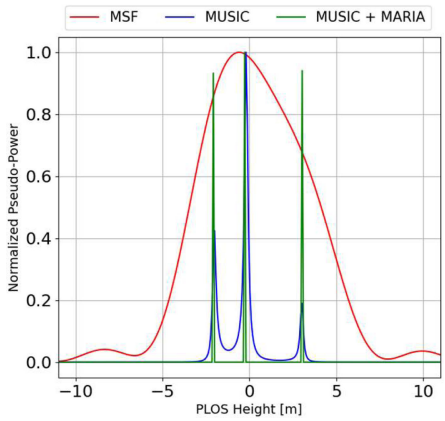

Fig. 3. Retrieved PSP after applying MSF (red), MUSIC (blue), MUSIC + MARIA (green). A SNR of 15 dB is set.

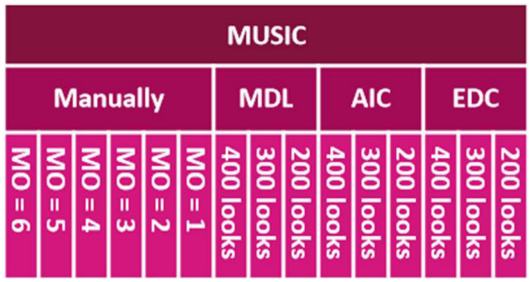

Fig. 4. Simulations made using MUSIC.

For a SNR of 15 dB, observe in Fig. 3 that only one phase-center is detected through MSF, i.e., $\hat{\mathbf{b}} = \{\mathbf{A}^{+}\mathbf{Y}\mathbf{A}\}_{\mathrm{diag}}$ [1, (eq. 6.3.18)], whereas MUSIC (utilizing EDC as MOS tool) and the proposed approach [MUSIC (using EDC) + MARIA] are able to discriminate all three phase-centers. The number and locations of the point-type-like targets (along the PLOS height direction) are chosen with the aim of demonstrating the super-resolution capabilities of MUSIC and MARIA, in contrast to the conventional MSF. The targets are placed close to each other and unevenly spaced, with the objective of stressing these methods out.

In order to quantify the quality of attained results, the next metrics are used:

1) *RMSE:* When all three phase-centers are discriminated, the RMSE between the true locations $\dot{\mathbf{z}}$ and the ones found $\hat{\dot{\mathbf{z}}}$ is calculated via

$$\mathrm{RMSE}\left(\dot{\mathbf{z}}, \hat{\dot{\mathbf{z}}}\right) = \sqrt{\sum_{i=1}^{I} \frac{\left(\dot{z}_i - \hat{\dot{z}}_i\right)^2}{I}}. \tag{26}$$

2) *DR:* It accounts for the number of times that all three phase-centers are distinguished. For the sake of avoiding false detections, we look for local maxima above a threshold value of 0.05 within the retrieved normalized (0 to 1) pseudopower. With the same aim, those trials with RMSE larger than 1.5 m are ignored, since they

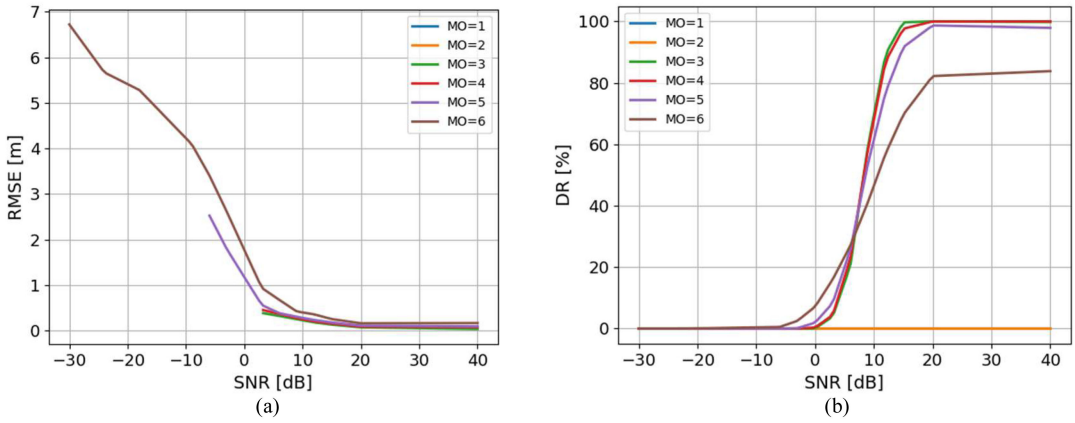

Fig. 5. Results achieved by MUSIC for all possible MOs. (a) Average RMSE against SNR. (b) DR against SNR.

are considered failure. With these considerations, Fig. 3 represents, by instance, a successful trial of MUSIC and MARIA.

A. Results Obtained by MUSIC

Employing MUSIC as focusing technique, we make use of three different MOS tools (i.e., AIC, MDL, and EDC) for comparisons. Since these tools require the amount of looks J in (7) as a priori information, we refer to three different approximations (i.e., 200, 300, and 400 looks) in order to study the influence of such a parameter. Recall that the actual number of looks for the reported simulations equals 300. Additionally, MUSIC is tested for all possible MOs (1 to 6) with the goal of showing the different responses. Fig. 4 summarizes the simulations made using MUSIC.

For each combination exhibited in Fig. 4, 800 Monte-Carlo simulations are performed for each succeeding representative SNR: -30; -24; -18; -9; -6; -3; 0; 3; 6; 9; 12; 15; 20; and 40 dB. Hence, MUSIC contributes with 168 000 simulations, since (3 MOS rules $\times$ 3 different number of looks $\times$ 14 SNRs $\times$ 800 Monte Carlo trials) + (6 MOs $\times$ 14 SNRs $\times$ 800 Monte Carlo trials) = 168 000.

Fig. 5 depicts the results obtained by MUSIC for all different possible MOs. Note that for some SNRs, the average RMSE in Fig. 5(a) does not appear, since all three targets are not detected, making the computation of the RMSE, as defined in (26), unfeasible. Whilst Fig. 5(b), at right hand, discards those trials where the RMSE is above 1.5 m.

In compliance with the theory, the best MO corresponds to three, i.e., the actual number of targets. Conversely, those MOs below three retrieve worst results due to underfitting, with a DR of 0%. On the other hand, the fourth and fifth MOs present similar performance as the third MO. Observe Fig. 5(b), the third, fourth and fifth MOs ensue in similar monotonically increasing curves with two main zones, one from -30 dB to ca. 0 dB, with a DR of about 0%, and another one from ca. 15 dB to 40 dB, with a DR near to 100%. Contrasting this behavior, the sixth MO does not approach 100% of DR but ca. 85%, while the first zone with 0% of DR is smaller, followed by a slower (wider) transition zone in the middle of the curve. In general, the transition zones of the curves aforementioned, from ca. 0 dB to ca.15 dB, present a RMSE below 1.5 m.

Based on Fig. 5, we conclude the following: (i) the performance of MUSIC is highly susceptible to the SNR; (ii) besides the third MO, models with relatively larger orders (i.e., 4 and 5) also retrieve good-fitted responses for higher SNRs.

Figs. 6–8 show the results retrieved by MUSIC for the treated MOS rules: AIC; MDL; and EDC, respectively. Observe that utilizing different approximations to the actual number of looks J in (7), for all addressed MOS rules, does not have significant influence in the results, especially for higher SNRs. Also, all MOS tools have better performance for SNRs above 15 dB, being EDC the only one approaching 100% of DR. In contrast, AIC and MDL attain a DR of ca. 85%. AIC and MDL tend to choose the largest MO, whereas EDC normally avoids it and rather selects the third, fourth and fifth MOs. Note in Figs. 6(a) and 7(a) that AIC and MDL still detect three targets below 9 dB, however, most of the time, these detections are ignored, since they are considered as false detections due to a RMSE above 1.5 m.

B. Results Obtained by MARIA

Next, we make use of MARIA as postprocessing step in order to enhance the responses of MUSIC for the experiments depicted in Fig. 4. Recall that the first and second MOs resulted in 0% DR, reason why, we do not consider them in the following simulations when selecting the MO manually (see Fig. 9). Hence, MARIA contributes with 145 600 simulations, since (3 MOS rules $\times$ 3 different number of looks $\times$ 14 SNRs $\times$ 800 Monte Carlo trials) + (4 MOs $\times$ 14 SNRs $\times$ 800 Monte Carlo trials) = 145 600.

With the aim of reducing computing time, the regularization parameter $\xi = N_0$ in (25) is calculated only once for each case described in Fig. 4 (ignoring the first and second MOs when chosen manually) and for each considered SNR. In principle, the results shown in the following could be improved by computing $\xi = N_0$ every time, i.e., for each trial. Also, MARIA's iterative procedure is finished by reaching ten iterations.

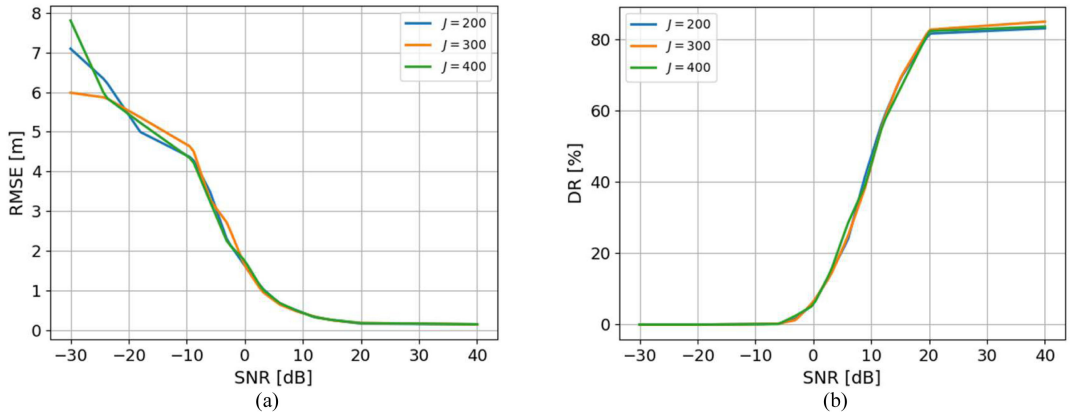

Fig. 6. Results achieved by MUSIC using AIC as MOS rule. (a) Average RMSE against SNR. (b) DR against SNR. Three different approximations to the actual number of looks J in (7) are considered: 200; 300; and 400.

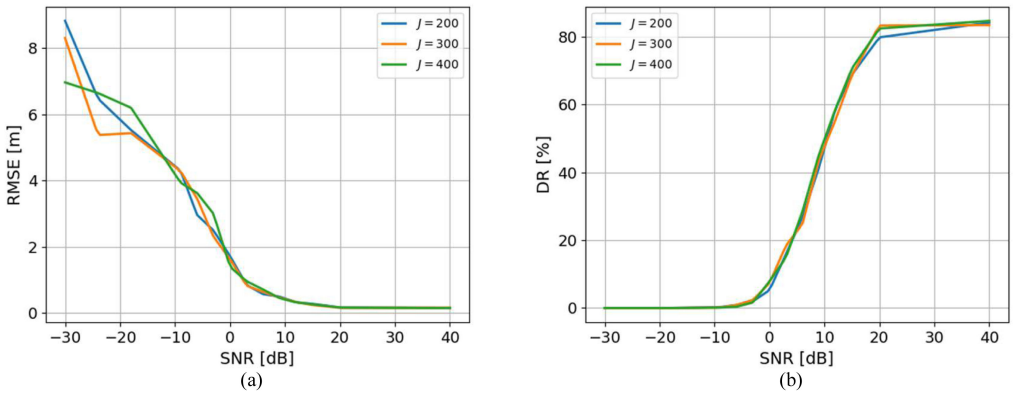

Fig. 7. Results achieved by MUSIC using MDL as MOS tool. (a) Average RMSE against SNR. (b) DR against SNR. Three different approximations to the actual number of looks J in (7) are considered: 200; 300; and 400.

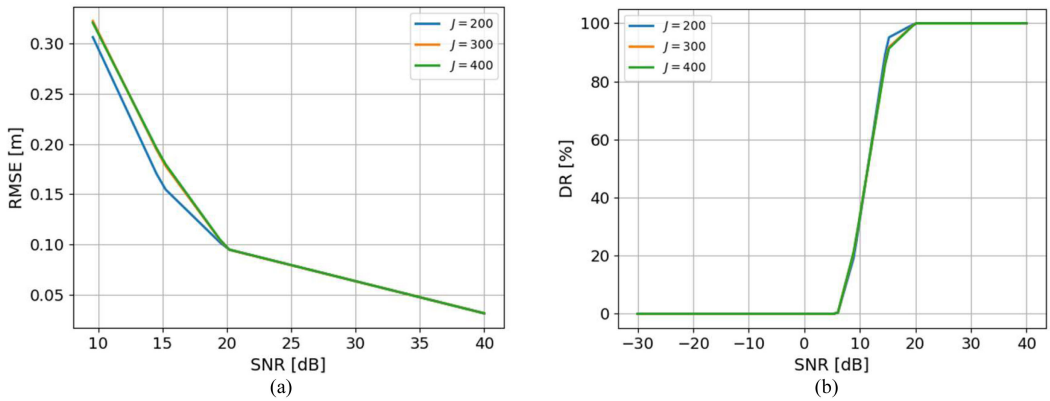

Fig. 8. Results achieved by MUSIC using EDC as MOS rule. (a) Average RMSE against SNR. (b) DR against SNR. Three different approximations to the actual number of looks J in (7) are considered: 200; 300; and 400.

Fig. 9 depicts the results obtained by MUSIC + MARIA for the considered MOs. In general, we can observe that the usage of MARIA as postprocessing step improves significantly the results achieved by MUSIC. The latter is especially notorious for SNRs below 9 dB. Observe in Fig. 9(b), how the curves attained by MUSIC in Fig. 5(b) have been moved to the left by ca. 25 dB. The variations in the middle of the curves, between -10 dB and 10 dB, are due to non-optimal regularization parameters $\xi = N_0$; this region in particular, resulted more susceptible to the (correct) choice of the regularization parameter.

The third, fourth, and fifth MOs recover similar results, whereas, the sixth MO presents worst performance. This behavior is consistent with Fig. 5, which depicts the inputs employed by MARIA. Yet, note in Fig. 9(b) that by incorporating MARIA

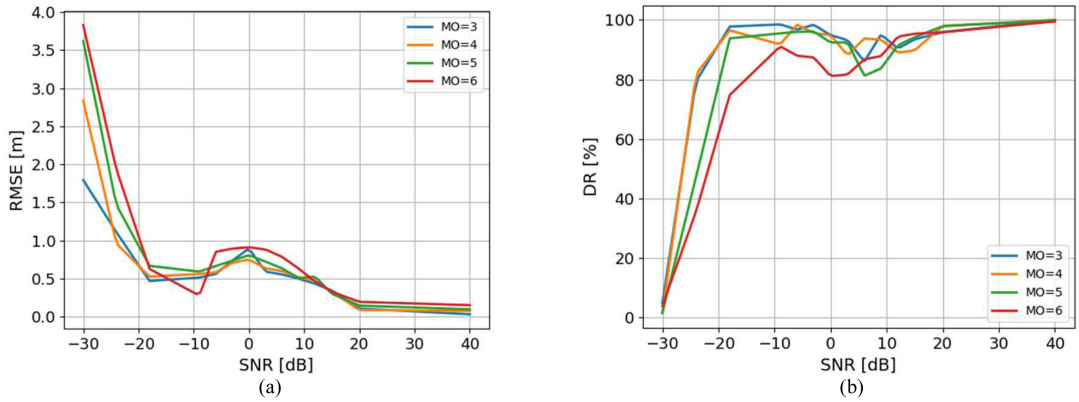

Fig. 9. Results achieved by MUSIC + MARIA for selected MOs. (a) Average RMSE against SNR. (b) DR against SNR.

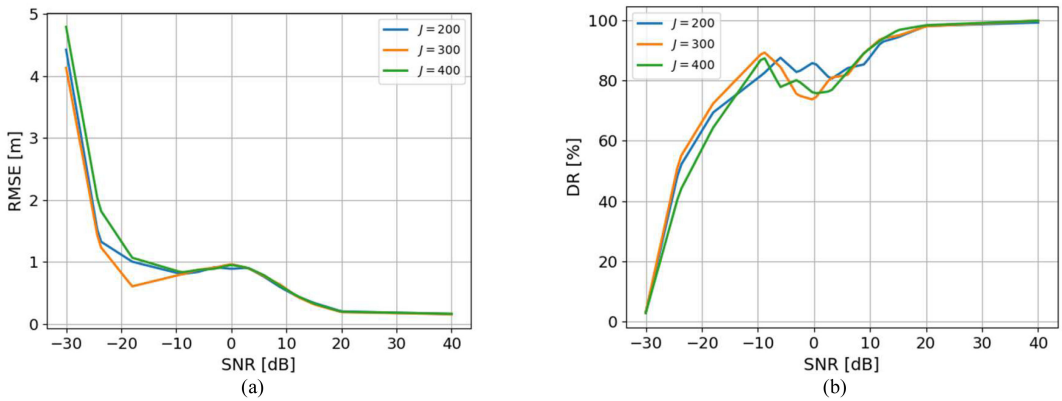

Fig. 10. Results achieved by MUSIC + MARIA using AIC as MOS rule. (a) Average RMSE against SNR. (b) DR against SNR. Three different approximations to the actual number of looks J in (7) are considered: 200; 300; and 400.

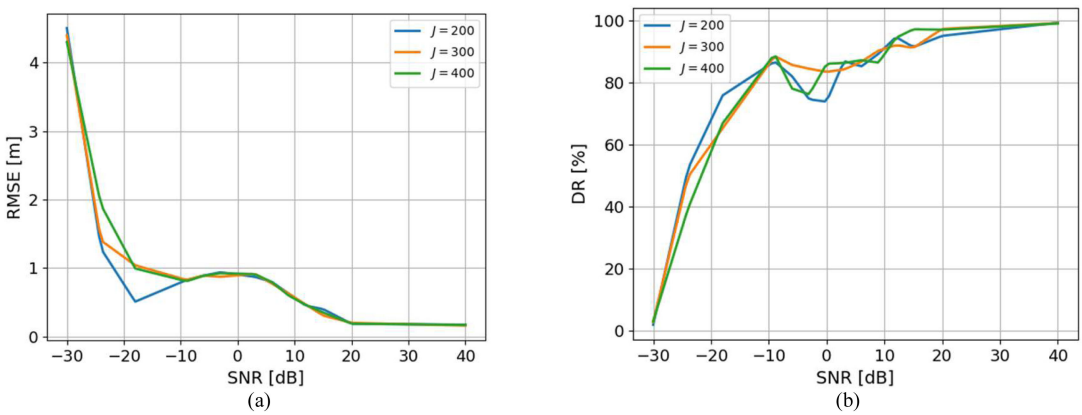

Fig. 11. Results achieved by MUSIC + MARIA using MDL as MOS tool. (a) Average RMSE against SNR. (b) DR against SNR. Three different approximations to the actual number of looks J in (7) are considered: 200; 300; and 400.

to MUSIC, the sixth MO approaches now 100% of DR for SNRs above 15 dB.

Figs. 10–12 show the results retrieved by MUSIC + MARIA for the addressed MOS rules: AIC; MDL; and EDC, correspondingly. As before, the utilization of different approximations to the number of looks J in (7), for the addressed MOS tools, does not have significant influence on the results. EDC in Fig. 12 seems more stable in comparison to AIC and MDL, attaining lower average RMSE and reaching a DR of ca. 100% for most SNRs. Yet, the metrics of EDC worsen abruptly for SNRs below −18 dB. Conversely, AIC and MDL retrieve similar results to each other, reaching ca. 100% of DR for SNRs above 15 dB. For SNRs below -18 dB, AIC and MDL retrieve better DR than EDC, having a slower transition to the zone of 0% DR.

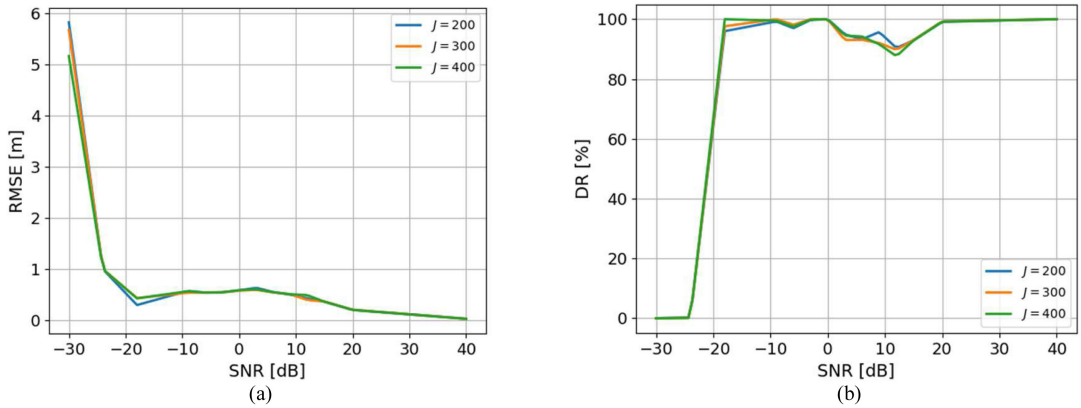

Fig. 12. Results achieved by MUSIC + MARIA using EDC as MOS rule. (a) Average RMSE against SNR. (b) DR against SNR. Three different approximations to the actual number of looks J in (7) are considered: 200; 300; and 400.

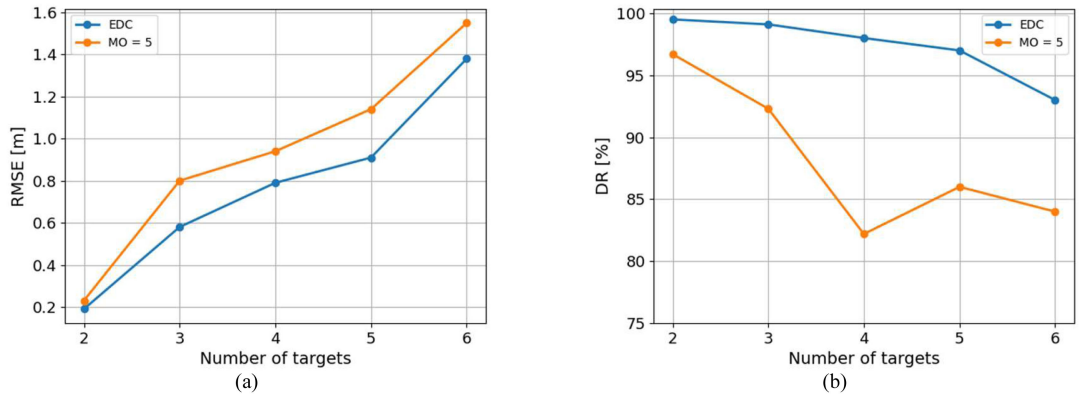

Fig. 13. Results achieved by MUSIC + MARIA using EDC as MOS rule and selecting the fifth MO manually. A SNR of 0 dB is set. (a) Average RMSE against number of targets. (b) DR against number of targets.

MARIA enhances the performance of MUSIC when the regularization parameter $\xi = N_0$ is properly set; nevertheless, it has the tradeoff of requiring more processing time. In average, the computation of a single trial takes MUSIC about 0.23 s, whereas MUSIC + MARIA entails about 0.72 s, i.e., approximately three times more. The measurements are performed in an Intel Xeon Gold 6154 CPU at 3.70GHz, using a single thread.

The addressed MOS rules perform well, partly due to its propensity to choose relatively large MOs. In addition, they contain a term that penalizes the highest MO, which attains poorer responses. Yet, AIC and MDL still tend to select the highest MO, retrieving, sometimes, misleading solutions. As an alternative to MOS tools, this article suggests choosing (manually) a large MO to perform focusing via parametric techniques like MUSIC. The highest MO, however, must be avoided. Afterward, regularization via MARIA is applied, seeking to attain good-fitted solutions.

Fig. 9 shows that the fourth and fifth MOs achieve similar performance as the best eligible MO (i.e., the actual number of targets). Therefore, as a rule of thumb, we recommend selecting the MO immediately below the highest MO; in this case, the fifth MO.

An illuminated region is normally composed of zones with different number of targets; thus, in the simulations presented next, we include additional cases of study. First, the SNR is set to 0 dB, since the capabilities of MARIA for improving performance with low SNRs are already demonstrated. Next, different number of point-type-like targets are considered. The simulations are performed as explained at the beginning of this section, with phase-centers placed at $\dot{z}_1 = -2$ m, $\dot{z}_2 = 0$ m, $\dot{z}_3 = 3$ m, $\dot{z}_4 = 6$ m, $\dot{z}_5 = 8$ m, and $\dot{z}_6 = 11$ m. The first case of study considers the first two phase-centers, the second case of study considers the first three phase-centers, and so on. For comparison purposes, we also present the results achieved using EDC (with $J = 300$), the MOS rule with best performance in the previous reported simulations. With this, 6400 simulations are added to this article.

Fig. 13 addresses the results attained for different number of targets. Observe that selecting the MO manually performs relatively well for the first three cases of study, with RMSE below 1 m and DR above 80%. The RMSE increases with the number of targets, whereas, the DR decreases. Note that when five targets are considered, there is an improvement of DR. This is expected, since the MO equals the actual number of targets. In

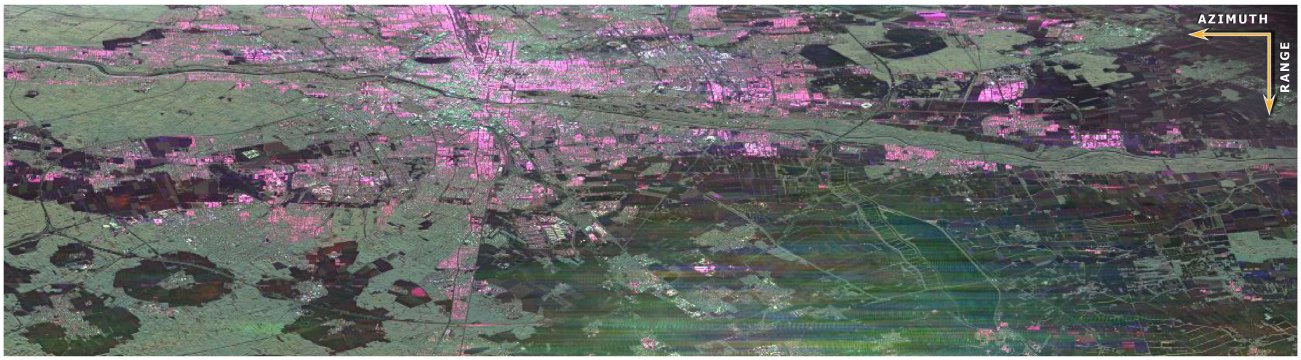

Fig. 14. SLC SAR image of the test site in Munich, Germany, 2015 (near range on top). The colors correspond to the channels HH (red), VV (blue) and HV (green).

general, the performance of EDC is significantly better, having more stable results for all different number of targets; the DR, by instance, stays above 90%.

Based on these results, we recommend using EDC as MOS rule instead of choosing the MO manually. Selecting the fifth MO by hand might attain good performance in some scenarios; nonetheless, choosing the same MO does not seem to be appropriate all the time. Conversely, the MO selected by MOS tools like EDC varies with the characteristics of the scene.

VII. Experimental Results

This section makes use of real data provided by the Jet Propulsion Laboratory (JPL) and the National Aeronautics and Space Administration (NASA). The dataset gathers L-band fully-polarimetric TomoSAR data collections from Munich (the third largest city in Germany), acquired by the UAVSAR system in 2015 [12], [13], [24]. The aircraft (Gulfstream G-III) flew at a nominal altitude of 12.5 km with a swath of 22 km and length of 60 km. The incidence angles range from 25° to 65°. The noise equivalent sigma-zero ranges from -35 dB to -53 dB across the swath [25]. For the specified microwave frequency band, with 0.24 m wavelength and 80 MHz chirp bandwidth, the resultant SLC imagery has a resolution of 1.66 m in range and 0.8 m in azimuth. Fig. 14 shows one SLC image out of the stack; the presence of radio frequency interference is due to the several external sources, by instance, those coming from Munich's airport. The TomoSAR acquisition geometry consists of seven passes at different altitudes, as given in Table I. These were completed on a heading of 193°. The expected vertical Fourier resolution is of about 2.8 m in near range and of about 6 m in far range.

For demonstration purposes, we define two ROI: the area where the building of the Bavarian state chancellery is located and the area where the Maximilianeum is placed. HH polarization is chosen due to the high intensity levels on these structures, as seen in Fig. 15, which depicts the corresponding intensity images with respect to the master track. The azimuth and range indices act as a guide to identify the bounds of each ROI, specified through the red rectangles. Note that the buildings are oriented practically parallel to the flight direction.

TABLE I
TomoSAR Acquisition Geometry

Track	Flight altitude [m]
1	12500
2	12500 + 30
3	12500 + 90
4	12500 + 160
5	12500 + 240
6	12500 + 400
7	12500 + 600

The tomograms presented afterward refer to the red lines crossing each ROI. Multilooking is performed on the set of data covariance matrices through Boxcar filtering, using a 5×10 (range/azimuth) pixel window. As a reference, we first apply MSF to focus the multilooked TomoSAR data. Next, MUSIC is computed via two approaches: choosing the MO manually (MO $= 5$) and with EDC as MOS tool. Finally, MARIA is applied with 10 iterations, employing as input, respectively, both results achieved previously by MUSIC.

With the aim of better appreciating the feature enhancing capabilities of MUSIC and MARIA (i.e., suppression of artifacts, ambiguity levels reduction and increased resolution), all their tomograms are normalized with respect to the (pseudo) power recovered using MSF, which is known to be more accurate in this aspect. The tomographic slices are presented in a dB scale, where 0 dB refers to the peak attained by MSF.

Fig. 16(a) shows the Google Earth image of the first test region, whereas Fig. 16(b) shows the respective polarimetric SLC SAR image [the colors correspond to the channels HH (red), VV (blue) and HV (green)]. Fig. 16(c) specifies the height of the different structures constituting the building of the Bavarian state chancellery. The corresponding tomograms are presented in Fig. 17 for HH polarization. For an easy assessment, Fig. 18 presents the superimposed vertical profiles for each azimuth

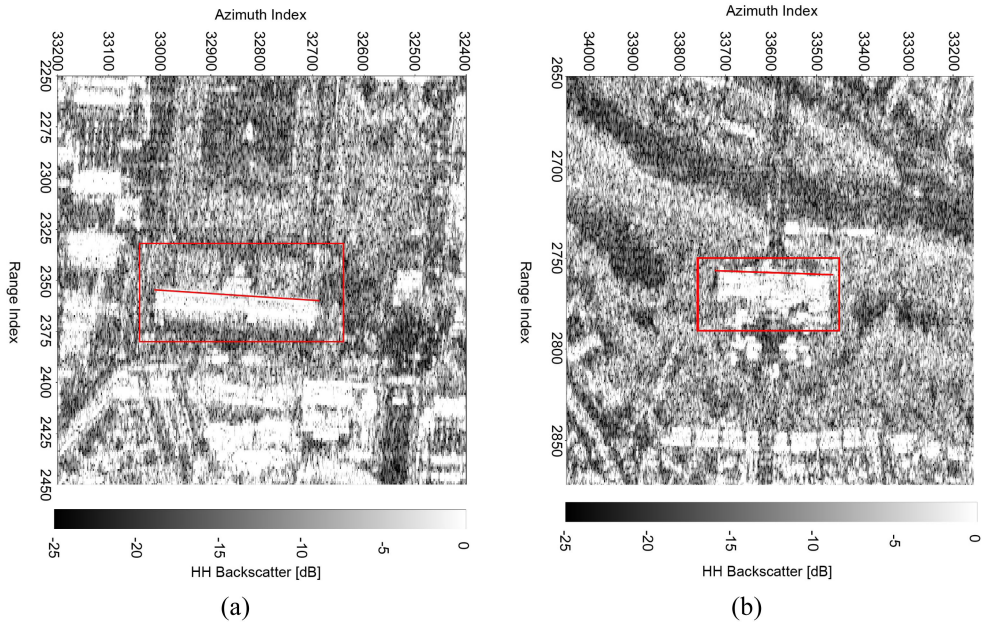

Fig. 15. Quick look intensity images of the two ROI for HH polarization. (a) Area where the building of the Bavarian state chancellery is located. (b) Area where the Maximilianeum is placed.

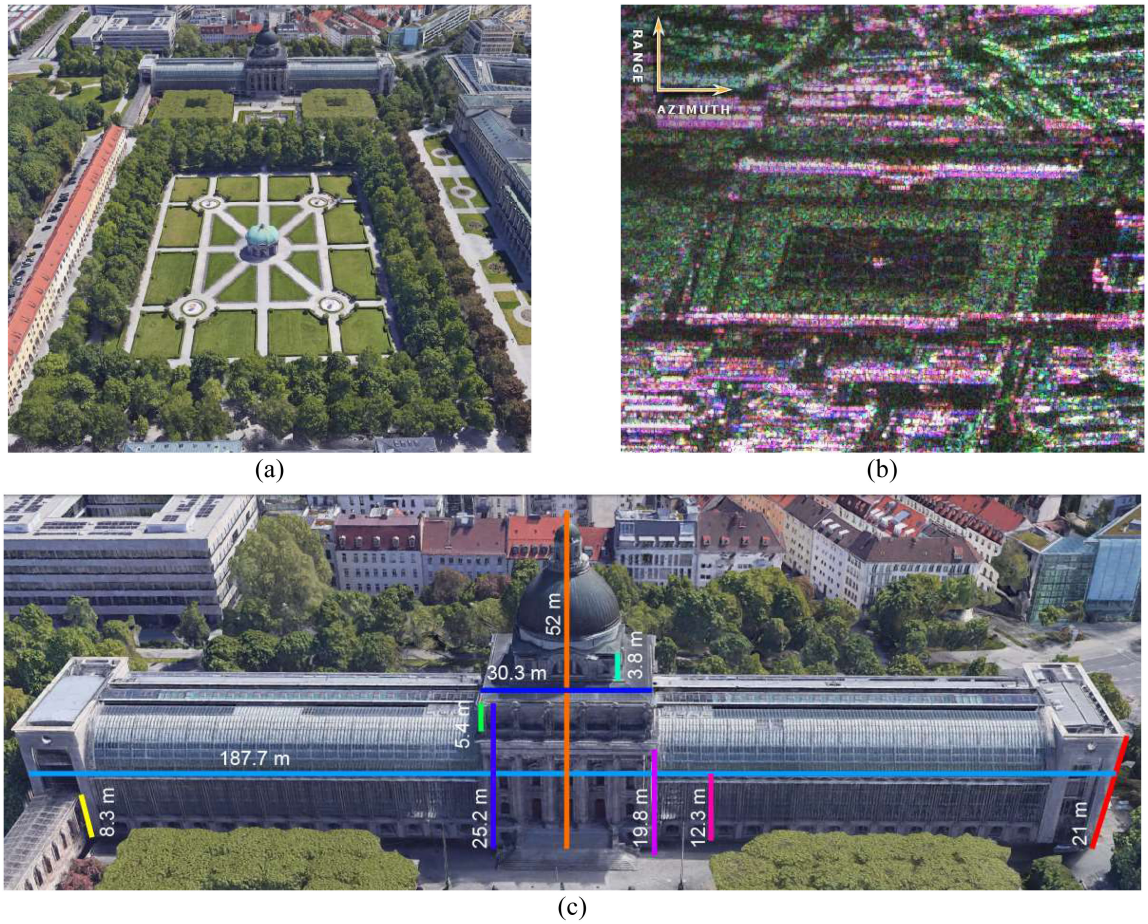

Fig. 16. (a) Google Earth image of the test region, where the building of the Bavarian state chancellery is located. (b) Polarimetric SLC SAR image of the test area [the colors correspond to the channels HH (red), VV (blue) and HV (green)]. (c) Front view of the edifice (Google Earth), specifying the height of the structures that constitute it.

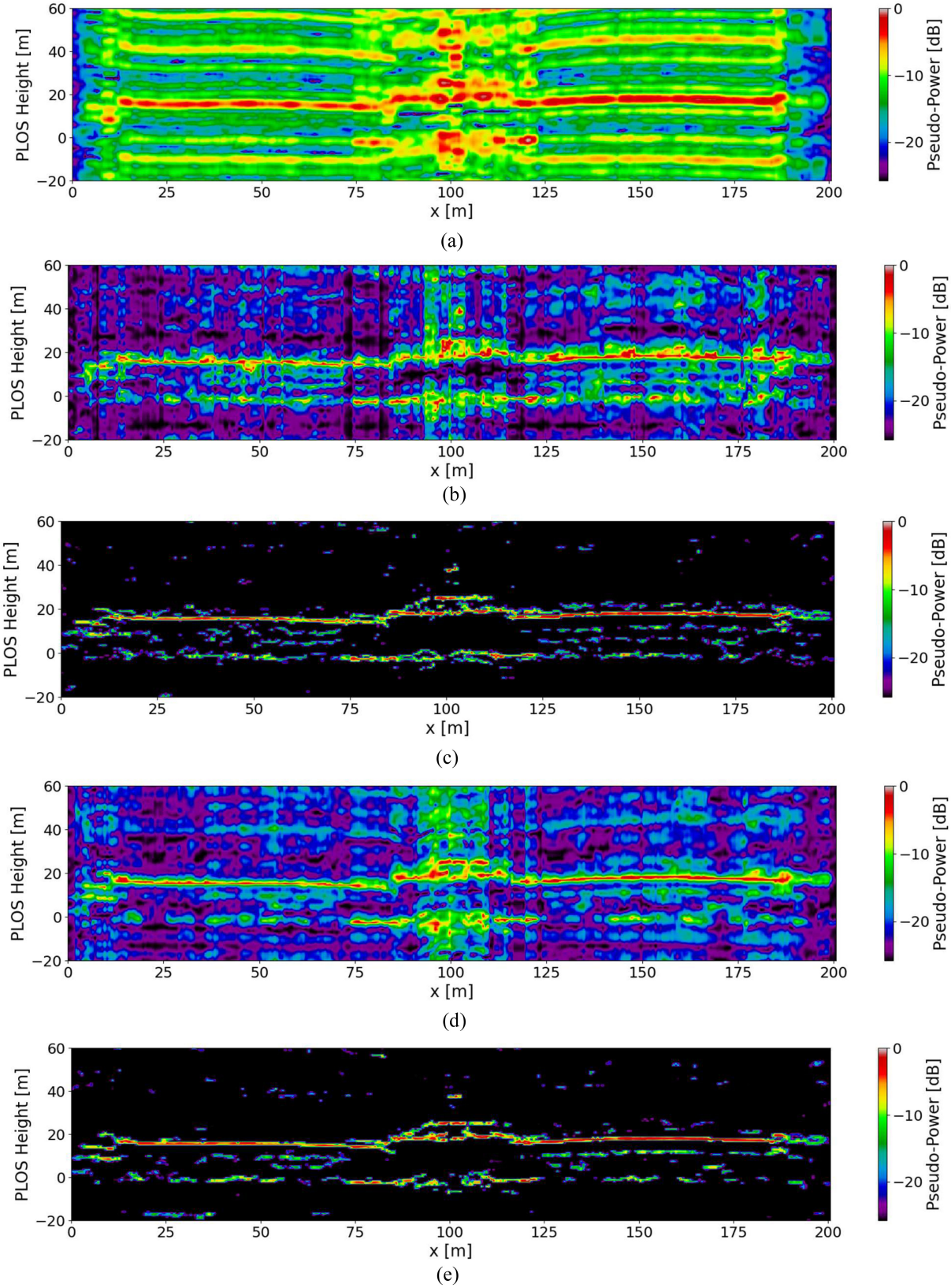

Fig. 17. HH tomograms retrieved from the area depicted by the red line crossing the ROI specified in Fig. 15(a). We perform focusing using (a) MSF, (b) MUSIC, selecting the MO manually (MO = 5), (c) MARIA with (b) as input, (d) MUSIC, using EDC as MOS tool, and (e) MARIA, with (d) as input.

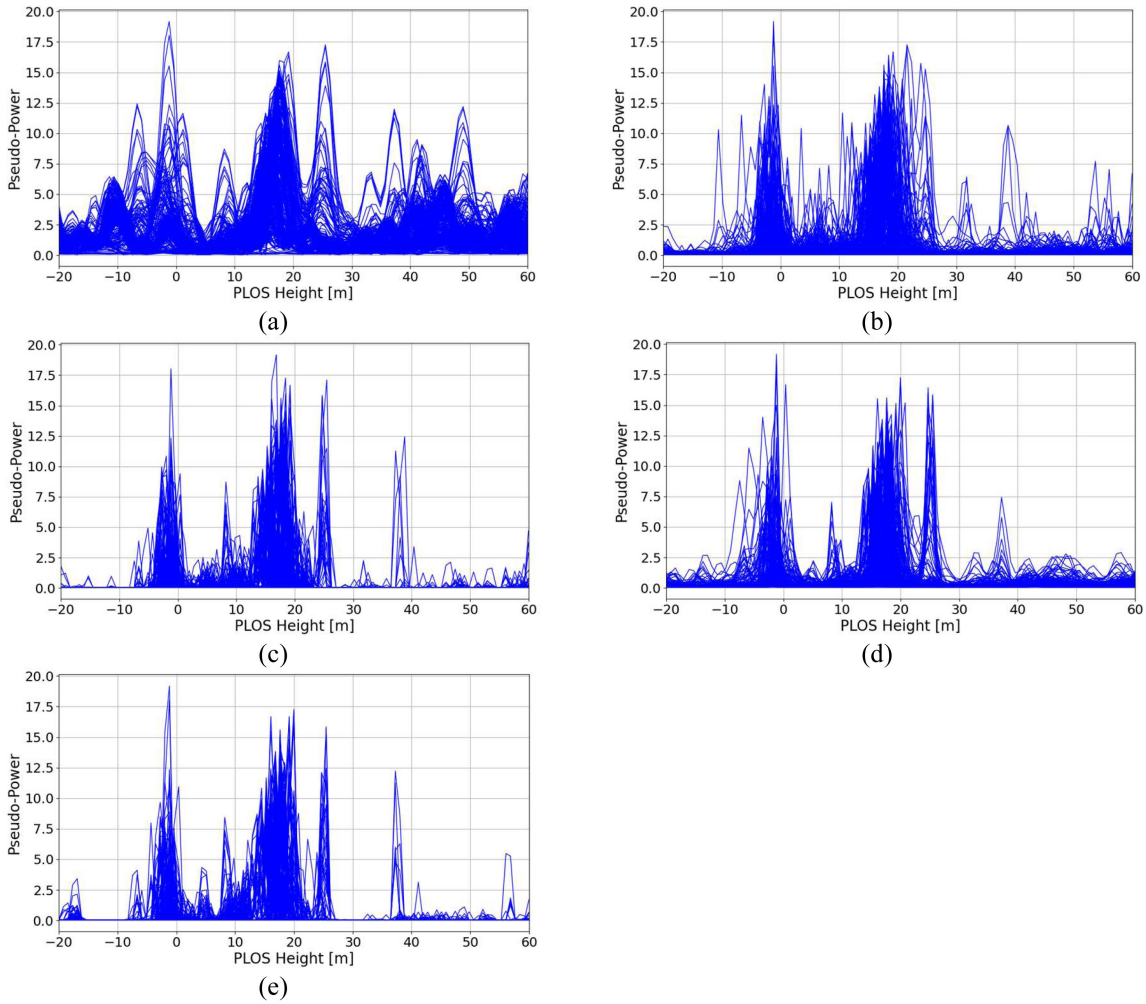

Fig. 18. Superimposed vertical profiles of the tomograms displayed in Fig. 17. (a) Matched spatial filtering, (b) MUSIC, selecting the MO manually (MO = 5), (c) MARIA with (b) as input, (d) MUSIC, using EDC as MOS tool, and (e) MARIA, with (d) as input. The (pseudo) power is presented in a linear scale.

position within the displayed tomograms; the (pseudo) power is presented in a linear scale.

As done before, Fig. 19(a) shows the Google Earth image of the second test region, Fig. 19(b) shows the respective polarimetric SLC SAR image and Fig. 19(c) specifies the height of the different structures constituting the Maximilianeum. The corresponding tomograms are depicted in Fig. 20 for HH polarization, whereas Fig. 21 presents the superimposed vertical profiles for each azimuth position within the respective tomograms.

Observe the tomograms attained by MSF in Figs. 17(a) and 20(a), the presence of high ambiguity levels (above and below the buildings), along with the lower resolution, hampers the interpretation of the results. Conversely, the tomographic slices attained by MUSIC and MARIA confirm their aforementioned feature enhancing capabilities.

In the case of MUSIC, choosing the MO manually [see Figs. 17(b) and 20(b)] performs relatively well. However, there is risk of over-fitting; targets may appear where in reality there are none. Recall that a relatively large MO is selected. Employing EDC as MOS tool [see Figs. 17(d) and 20(d)], on the other hand, prevents over-fitting through a penalty term, as defined in (21). EDC selects the most proper MO for each azimuth position along the tomogram, according to the criteria explained previously in Section IV.

For different inputs, MARIA aims to attain a unique solution to the TomoSAR problem [see Fig. 17(c) and (e); and Fig. 20(c) and (e)]. However, this goal can be achieved until certain extent, as it depends on how different the inputs are. Nevertheless, it is recommended utilizing MARIA as postprocessing step, seeking to correct the imprecisions that the tomograms recovered by MUSIC may have.

Most of the structures constituting both edifices (i.e., the Bavarian state chancellery and the Maximilianeum) are distinguished more easily in the tomographic slices retrieved by MARIA. By instance, observe in the first case, the two wings (one at each side), the central building and part of the dome. For the second edifice, observe the two towers at the extremes, both wings (one at each side) and the central building. Although MUSIC is considered as a super-resolution technique, their results can be still improved through MARIA, at the expense of more processing time (about three times more). The presented

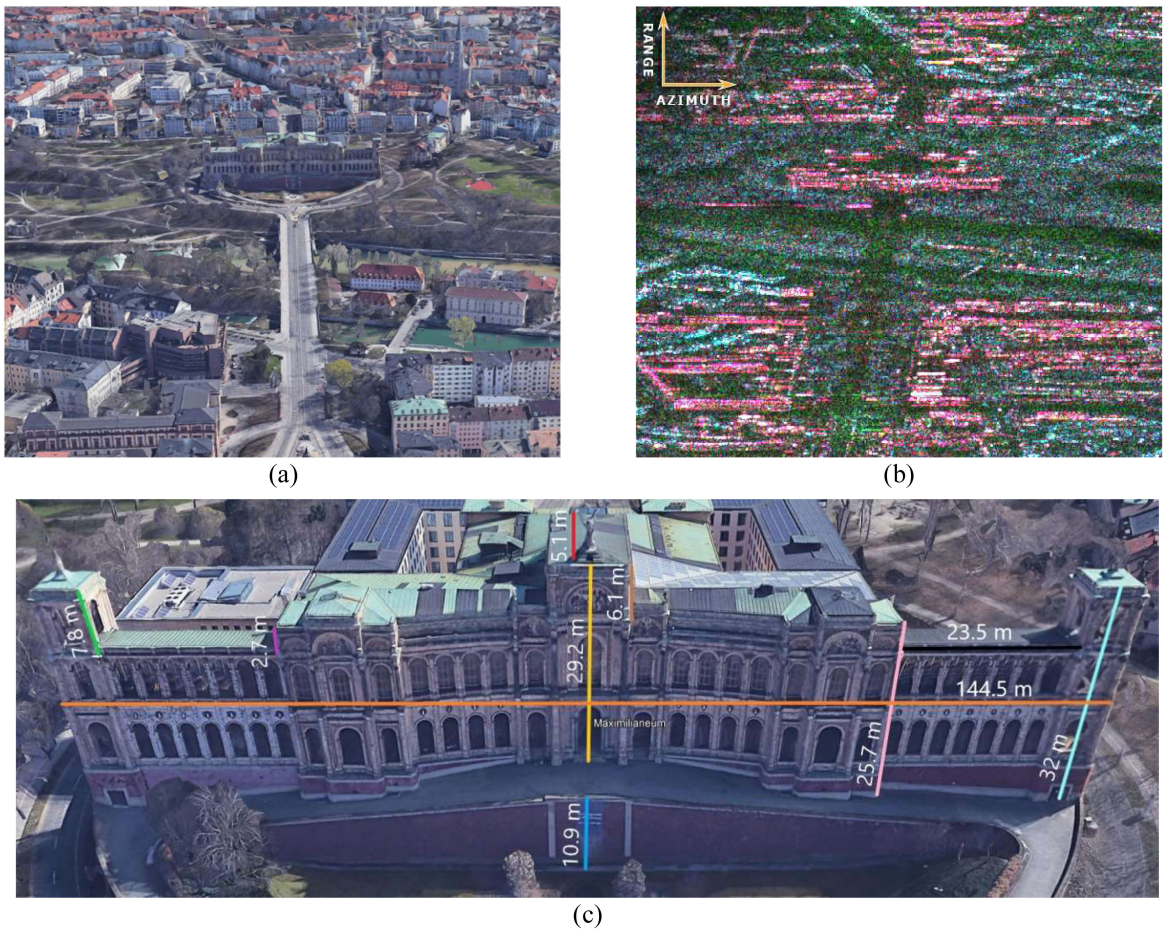

Fig. 19. (a) Google Earth image of the test region, where the Maximilianeum building is located. (b) Polarimetric SLC SAR image of the test area [the colors correspond to the channels HH (red), VV (blue) and HV (green)]. (c) Front view of the Maximilianeum edifice (Google Earth), specifying the height of the structures that constitute it.

experimental results verify then the successful implementation of the strategy proposed in Fig. 1.

VIII. Conclusion

As done with nonparametric techniques in previous related studies [10]–[13], this article shows that MARIA also refines the solutions attained by parametric methods like MUSIC. In contrast to non-parametric methods, an intermediate step is needed: the selection of the MO, which can be done manually or via MOS tools (e.g., AIC, MDL, or EDC), most of them based on theoretic information criteria.

According to the reported simulations, MUSIC performs well for higher SNRs (in this case, above 15 dB), necessitating a regularization postprocessing step just for scenarios with low SNR. Consequently, since using MARIA requires of (about three times) more processing time, it should be employed only in adverse scenarios with low SNR and when the degree of detail is particularly important. Focusing of illuminated areas could be then done with MUSIC in some zones, whereas in another MARIA could be incorporated.

Simulation results show that having different approximations to the actual number of looks J in (7), seems not to affect the performance of the addressed MOS rules. EDC appears as the more accurate MOS tool, having AIC and MDL similar performance to each other.

Selecting manually a relatively large MO and, afterward, combining MUSIC with MARIA, is also a plausible option seeking to retrieve good-fitted results and achieving feature enhancement. Yet, the performance with EDC is significantly better.

The experimental results in Section VII, verify the successful implementation of the strategy proposed in Fig. 1 for a real case (urban) scenario. Using MARIA as a post-processing step, aids correcting the inaccuracies that the tomograms rertieved by MUSIC may have, since MARIA aims to attain a unique solution to the TomoSAR problem. Also, MARIA provides further enhancement (i.e., suppression of artifacts, ambiguity levels reduction and increased resolution) to the solutions achieved by MUSIC, easing the interpretation of the results.

Tackling the spatial spectral estimation problem within the context of DOA, allows using novel strategies as the one described in Fig. 1. For demonstration purposes, TomoSAR has acted as an application. Nonetheless, keep in mind that the proposed approach can be adapted to different applications, which also deal with the problem of determining how the

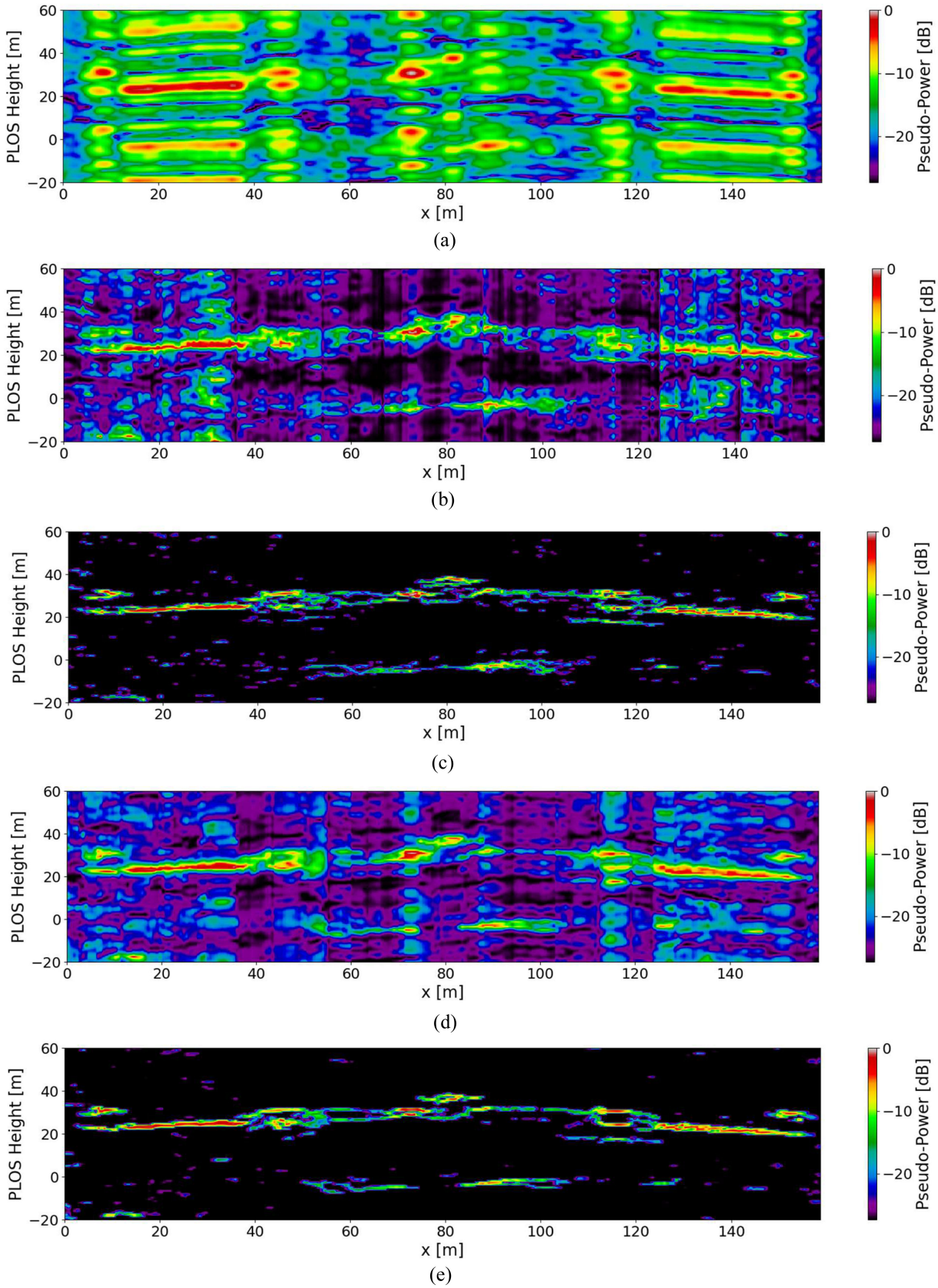

Fig. 20. HH tomograms retrieved from the area depicted by the red line crossing the ROI specified in Fig. 15(b). We perform focusing using (a) Matched spatial filtering, (b) MUSIC, selecting the MO manually (MO = 5), (c) MARIA with (b) as input, (d) MUSIC, using EDC as MOS tool, and (e) MARIA, with (d) as input.

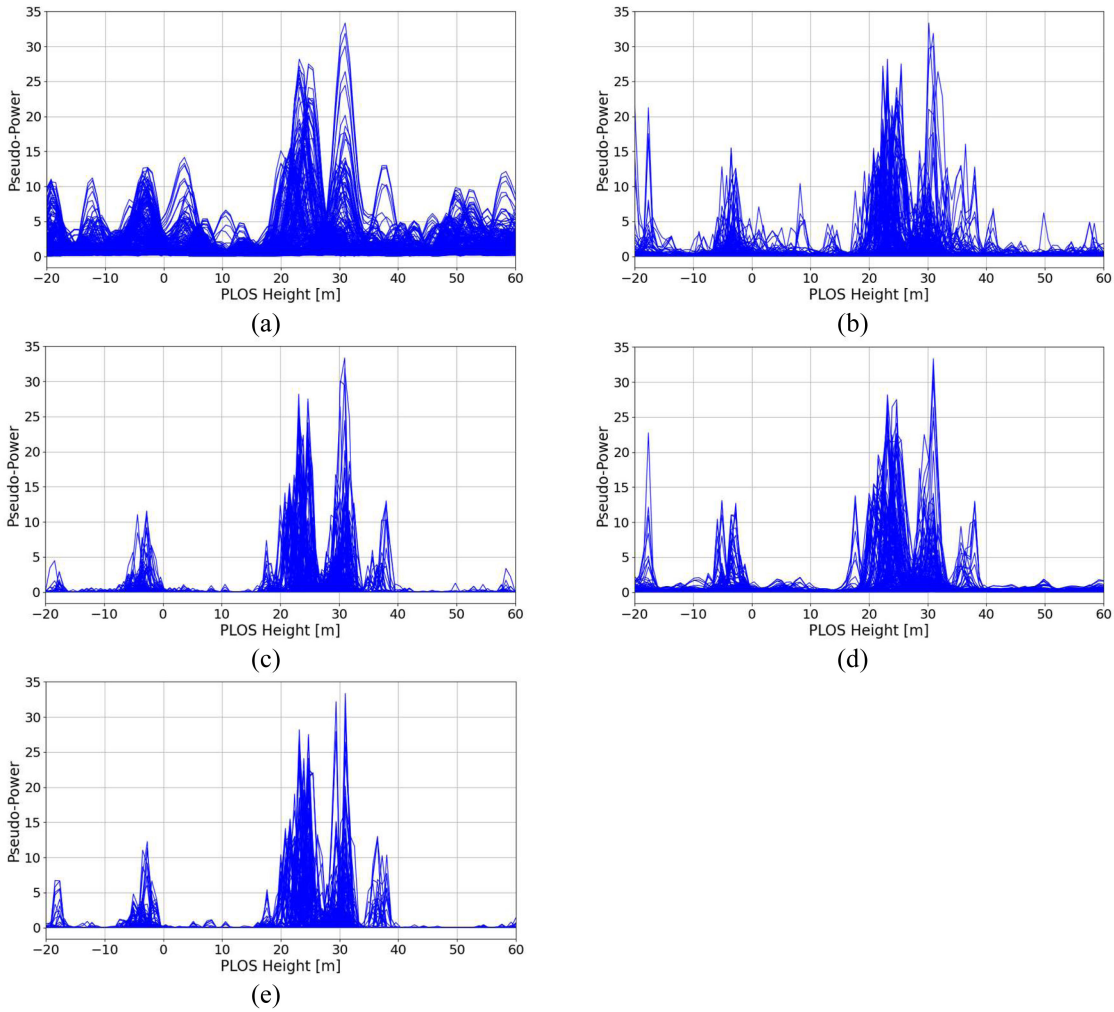

Fig. 21. Superimposed vertical profiles of the tomograms displayed in Fig. 20. (a) Matched spatial filtering, (b) MUSIC, selecting the MO manually (MO = 5), (c) MARIA with (b) as input, (d) MUSIC, using EDC as MOS tool, and (e) MARIA, with (d) as input. The (pseudo) power is presented in a linear scale.

energy is distributed over space. This includes a variety of fields, e.g., sonar, telecommunications, biomedical engineering, and seismology.

ACKNOWLEDGMENT

The authors would like to thank Dr. S. Hensley from the JPL/NASA, for providing the UAVSAR data utilized in the reported experiments.

REFERENCES

[1] P. Stoica and R. L. Moses, *Spectral Analysis of Signals*, vol. 1, Upper Saddle River, NJ, USA: Prentice-Hall, 2005.

[2] M. Nannini, R. Scheiber, R. Horn, and A. Moreira, "First 3-D reconstructions of targets hidden beneath foliage by means of polarimetric SAR tomography," *IEEE Geosci. Remote Sens. Lett.*, vol. 9, no. 1, pp. 60–64, Jan. 2012.

[3] A. Saucan, C. Sintes, T. Chonavel and J. L. Caillec, "Model-based adaptive 3D sonar reconstruction in reverberating environments," *IEEE Trans. Image Process.*, vol. 24, no. 10, pp. 2928–2940, Oct. 2015.

[4] S. Li, Y. Liu, L. You, W. Wang, H. Duan, and X. Li, "Covariance matrix reconstruction for DOA estimation in hybrid massive MIMO systems," *IEEE Wireless Commun. Lett.*, vol. 9, no. 8, pp. 1196–1200, Aug. 2020.

[5] N. Dey, A. S. Ashour, F. Shi, and R. S. Sherratt, "Wireless capsule gastrointestinal endoscopy: Direction-of-arrival estimation based localization survey," *IEEE Rev. Biomed. Eng.*, vol. 10, pp. 2–11, Apr. 2017.

[6] S. Rost and C. Thomas, "Array seismology: Methods and applications," *Rev. Geophys.*, vol. 40, no. 3, pp. 1–27, Sep. 2002.

[7] P. Stoica and Y. Selen, "Model-order selection: A review of information criterion rules," *IEEE Signal Process. Mag.*, vol. 21, no. 4, pp. 36–47, Jul. 2004.

[8] M. Wax and T. Kailath, "Detection of signals by information theoretic criteria," *IEEE Trans. Acoust., Speech, Signal Process.,* vol. 33, no. 2, pp. 387–392, Apr. 1985.

[9] F. Lombardini and F. Gini, "Model order selection in multi-baseline interferometric radar systems," *EURASIP J. Adv. Signal Process.,* vol. 2005, no. 20, pp. 3206–3219, 2005.

[10] G. Martín del Campo, M. Nannini, and A. Reigber, "Statistical regularization for enhanced TomoSAR imaging," *IEEE J. Sel. Topics Appl. Earth Observ. Remote Sens.*, vol. 13, pp. 1567–1589, Feb. 2020.

[11] G. Martín del Campo, M. Nannini, and A. Reigber, "Towards feature enhanced SAR tomography: A maximum-likelihood inspired approach," *IEEE Geosci. Remote Sens. Lett.*, vol. 15, no. 11, pp. 1730–1734, Nov. 2018.

[12] G. D. Martín-del-Campo-Becerra, S. A. Serafín-García, A. Reigber and S. Ortega-Cisneros, "Parameter selection criteria for Tomo-SAR focusing," *IEEE J. Sel. Topics Appl. Earth Observ. Remote Sens.*, vol. 14, pp. 1580–1602, Jan. 2021.

[13] G. D. Martín-del-Campo-Becerra, A. Reigber, M. Nannini, and S. Hensley, "Single-look SAR tomography of urban areas," *Remote Sens.*, vol. 12, Aug. 2020, Art. no. 2555.

[14] Y. Huang, L. Ferro-Famil, and A. Reigber, "Under-Foliage object imaging using SAR tomography and polarimetric spectral estimators," *IEEE Trans. Geosci. Remote Sens.*, vol. 50, no. 6, pp. 2213–2225, Jun. 2012.
[15] F. Gini, F. Lombardini, and M. Montanari, "Layover solution in multibaseline SAR interferometry," *IEEE Trans. Aerosp. Electron. Syst.*, vol. 38, no. 4, pp. 1344–1356, Oct. 2002.
[16] H. H. Barrett and K. J. Myers, *Foundations of Image Science.* New York, NY, USA: Willey, 2004.
[17] M. Schmitt and U. Stilla, "Maximum-likelihood-based approach for single-pass synthetic aperture radar tomography over urban areas," *IET RadarSonar Navig.*, vol. 8, no. 9, pp. 1145–1153, Apr. 2014.
[18] H. L. Van Trees, *Optimum Array Processing: Part IV of Detection, Estimation, and Modulation Theory.* New York, NY, USA: Wiley, 2004.
[19] G. Schwarz, "Estimating the dimension of a model," *Ann. Statist.*, vol. 6, no. 2 pp. 461–464, 1978.
[20] J. L. Mueller and S. Siltanen, *Linear and Nonlinear Inverse Problems with Practical Applications*. vol. 10, Philadelphia, PA, USA: SIAM, 2012.
[21] M. Bertero and P. Boccacci, *Introduction to Inverse Problems in Imaging*. Boca Raton, FL, USA: CRC Press, 1998.
[22] Y. V. Shkvarko, "Unifying regularization and Bayesian estimation methods for enhanced imaging with remotely sensed data—Part I and Part II," *IEEE Trans. Geosci. Remote Sens.*, vol. 42, no. 5, pp. 923–940, May 2004.
[23] Y. V. Shkvarko, "Unifying experiment design and convex regularization techniques for enhanced imaging with uncertain remote sensing data—Part I and Part II," *IEEE Trans. Geosci. Remote Sens.*, vol. 48, no. 1, pp. 82–111, Jan. 2010.
[24] S. Hensley *et al.*, "UAVSAR tomography of Munich," in *Proc. IEEE Int. Geosci. Remote Sens. Symp.*, 2019, pp. 1140–1143.
[25] C. E. Jones, B. Minchew, B. Holt, and S. Hensley, "Studies of the deepwater horizon oil spill with the UAVSAR radar," in *Monitoring and Modeling the Deepwater Horizon Oil Spill: A Record-Breaking Enterprise*. Y. Liu, A. MacFadyen, Z.-G. Ji, and R. H. Weisberg, Eds., Washington, DC, USA: AGU. pp. 33–50, Aug. 2011.

Gustavo Daniel Martín-del-Campo-Becerra received the Engineering degree in electronics and communications engineering from the University of Guadalajara, Guadalajara, Jalisco, Mexico, in 2008, and the M.Sc. and Dr.Sc. (Ph.D. equivalent) degrees in electrical engineering, with specialization in telecommunications from the Center for Research and Advanced Studies, National Polytechnic Institute, Guadalajara, Jalisco, Mexico, in 2013 and 2017, respectively.

Since 2017, he has been with the Microwaves and Radar Institute, German Aerospace Center. His research interests include the applications of signal processing to remote sensing, particularly SAR tomography, inverse problems, random fields estimation, and adaptive spatial analysis.

Sergio Alejandro Serafín-García received the Engineering degree in electronics and communications engineering from the University of Guadalajara, Guadalajara, Jalisco, Mexico, in 2017, and the M.Sc. degree in electrical engineering, with specialization in telecommunications from the Center for Research and Advanced Studies, National Polytechnic Institute, Guadalajara, Jalisco, Mexico, in 2021.

His research interests include the applications of signal processing to remote sensing, particularly SAR tomography.

Andreas Reigber (Fellow, IEEE) received the Diploma degree in physics from the University of Konstanz, Konstanz, Germany, in 1997, the Ph.D. degree in engineering from the University of Stuttgart, Stuttgart, Germany, in 2001, and the Habilitation degree from the Berlin University of Technology, Berlin, Germany, in 2008.

He is currently the Head of the SAR Technology Department, Microwaves and Radar Institute (HR), German Aerospace Center, Weßling, Germany, where he is leading the development and operation of state-of-the-art airborne SAR sensors. He is currently a Professor of remote sensing and digital image processing with the Berlin University of Technology, Berlin, Germany. His research interests include various aspects of multimodal, multichannel, and high-resolution SAR processing and postprocessing.

Dr. Reigber was the recipient of several prize paper awards, among them the IEEE TGRS Transactions Prize Paper Award in 2001 and 2016 for his works on polarimetric SAR tomography and nonlocal speckle filtering, respectively, and also the IEEE TGRS Letters Prize Paper Award in 2006 for his work on multipass SAR processing.

Susana Ortega-Cisneros received the Engineering degree in electronics and communications engineering from the University of Guadalajara, Guadalajara, Jalisco, Mexico, in 1990, the M.Sc. degree in solid state electronics from the Center for Research and Advanced Studies, National Polytechnic Institute, Mexico City, Mexico, in 1995 and the Ph.D. degree in computer science and telecommunications from the Autonomous University of Madrid, Madrid, Spain, in 2005.

Since 2010, she has been with the Center for Research and Advanced Studies (Cinvestav), National Polytechnic Institute, Guadalajara, Jalisco, Mexico. She is involved in the design of digital architectures based on FPGAs, digital signal processors (DSPs), and microprocessors. Her current research interests include digital control, self-timed synchronization, electronic systems applied to biomedicine, embedded microprocessor design, digital electronics, custom DSPs in FPGAs, and, recently, remote sensing applications.

Matteo Nannini received the Laurea degree in telecommunication engineering from the University of Florence, Italy, in 2003. The thesis has been done in collaboration with the Microwaves and Radar Institute of the German Aerospace Center, and the Ph.D. degree in electrical engineering with a thesis on SAR tomography, from the Karlsruhe Institute of Technology, Karlsruhe, Germany, in 2009.

Since 2004, he has been with the Microwaves and Radar Institute of the German Aerospace Center, where he is working on SAR tomography, spectral estimation techniques, radar ice sounding, and PSI time series analysis. He is involved in several studies for the evaluation of the performance for future bi- and multistatic SAR missions.